d'Collection

Thesis for the Degree of Master of Science

Characterization of 20-inch Micro Channel Plate Photomultiplier Tubes

Department of Physics, Major in Particle Physics

The Graduate School

Geonwoo Kim

June 2022

The Graduate School
Kyungpook National University

Characterization of 20-inch Micro Channel Plate Photomultiplier Tubes

Geonwoo Kim

Department of Physics, Major in Particle Physics
The Graduate School

Supervised by Professor Hong Joo Kim

Approved as a qualified thesis of Geonwoo Kim
for the degree of Master of Science by the Evaluation Committee

June 2022

Chairman   Jik Lee   ㉑

             Jungsic Park   ㉑

             Hong Joo Kim   ㉑

The Graduate School Council
Kyungpook National University

Characterization of 20-inch Micro Channel Plate Photomultiplier Tubes*

Geonwoo Kim

Department of Physics, Major in Particle Physics

Graduate School, Kyungpook National University,

Daegu, Korea

(*Supervised by Professor Hong Joo Kim*)

Abstract

Cherenkov radiation refers to the radiation that is generated when charged particles travel in a medium and the speed of the particles is faster than the speed of light. To observe high-energy neutrinos by Cherenkov radiation, a very large amount of medium and large-area optical sensors are required. Korean Neutrino Observatory (KNO), a project proposed to detect neutrinos in Korea, is a observatory that installs tens of thousands of optical sensors deep underground in a large water tank. The 20-inch micro channel plate photomultiplier tube (MCP-PMT) is one of the photosensor options for use in the KNO because of its advanced properties, which include a wide optical area and good collection efficiency. A closer examination of the characteristics of such a large-area PMT is an important study for KNO or other experiment that observing big Cherenkov radiation. We have studied the characteristics of two 20-inch MCP-PMTs including single photoelectron's charge resolution, signal-to-noise ratio, gain, after-pulse ratio, dark count rate and timing performance. In addition, methods for measuring attributes has been devised and tested. Lastly, we compared the measurements of these characteristics with previous studies.

Contents

List of Figures

List of Tables

1

Introduction

There are numerous physical phenomena that emit light in nature, and technologies for observing them can be applied to physical experiments and other various fields. Photomultiplier tubes are devices capable of detecting light precisely enough to separate a single photoelectric signal and amplifying it among many devices for detecting light. The KNO is an experiment that detects water Cherenkov radiation generated by particles which is produced when neutrinos interact with substances in water, and requires tens of thousands of large-diameter photomultiplier tubes[1]. The purpose of this study is to investigate the characteristics of large-diameter micro channel plate photomultiplier tubes (MCP-PMTs) among devices designed to be used in experiments on this scale.

1.1   Neutrinos

Neutrinos are basic particles that make up the cosmos. They are formed as a result of beta decay, which is triggered by weak interactions. Neutrinos are characterized by very small mass, no charge, and little interaction with matter. The existence of neutrinos was predicted in the 1930s due to the facts that the electron spectrum caused by beta decay (in the 1910s and 1920s) was discovered as continuous spectrums rather than line spectrums and the law of conservation of momentum for beta decay was not established. Many experiments have discovered neutrinos since the predicted existence of neutrinos, in 1988 the discovery of muon neutrinos was awarded a Nobel Prize, and in 1995 the discovery of electron neutrinos was awarded a Nobel Prize. In 2002, a Nobel Prize awarded for the discovery of neutrinos coming from spacecraft, and in 2015, a Nobel Prize awarded for discovering the neutrino oscillation phenomenon in Super-Kamiokande[2] and SNO experiments[3]. The ques-

tions about current neutrinos are: What is the mass of neutrinos? Do neutrinos have different properties than antineutrinos? Are there other types of neutrinos? And so on.

1.2   Neutrino observatory using Cherenkov Radiation

When electrons move in a transparent medium, the atoms of the medium are polarized in the direction in which the electrons move by the electric field created by the electrons. The electric field created by this polarization does not produce electromagnetic waves when the particle is slow, but if the velocity of the particles is faster than the speed of light in the medium, the wavelets of the electromagnetic fields from all parts of the track can be generated to be in phase with each other. And according to Hoygens' principle, radiation can be seen at a certain angle; this phenomenon is known as Cherenkov radiation[4].
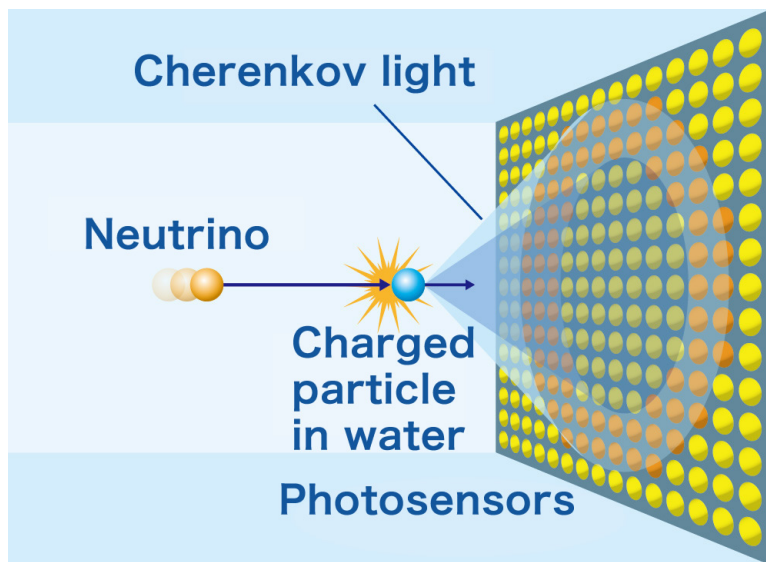
Figure 1.1: Cherenkov light[5].

Neutrinos are very difficult to detect because they rarely interact with matter. However, sometimes neutrinos can interact with nuclei or electrons, where electron neutrinos emit electrons and muon neutrinos emit muons. And since electrons and muons have a charge, they emit Cherenkov radiation in the medium if neutrinos interact with matter. To detect neutrinos in this way, a large-scale liquid medium such as water or ice was used, and a method was devised to position the detector deep underground to avoid interference by cosmic rays. Typical neutrino observatories

include Super-Kamiokande in Japan and Ice Cube Observatory in the South Pole[6], as well as Hyper-Kamiokande under construction in Japan[7]. There was also a proposal to build a neutrino observatory in South Korea. Both Hyper Kamiokande and
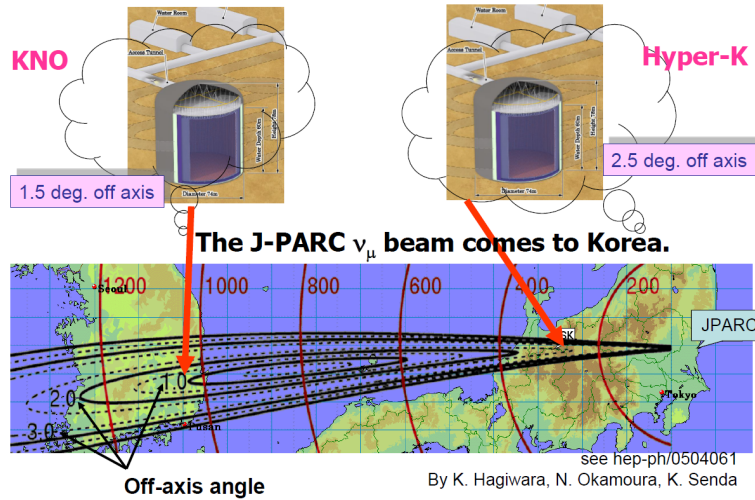
Figure 1.2: KNO and Hyper Kamiokande facility[8].

KNO construct the same 60-meter-high, 74-meter-diameter water tank. The volume totals 260 kton, whereas the fiducial volume is 190 kton. It covers 40% of the sensor area with 40,000 20-inch PMTs on the inside. By examining the oscillations of neutrinos sent from space and accelerators, we can determine the mixing angles and squared mass differences of neutrinos. Additionally, it would explain the imbalance between matter and antimatter.

1.3   Neutrino oscillation

Neutrinos are classified into three types: electron neutrinos, muon neutrinos, tau neutrinos, as well as anti-neutrinos. Tau neutrinos interact with tau particles, electron neutrinos interact with electrons, muon neutrinos interact with muons. Neutrinos oscillate between three distinct flavor states when they travel. Neutrinos fluctuate between flavor states as a result of neutrino mixing. While the neutrino oscillates, the three flavors may swap places. Even though the neutrino has the flavor of an electron, it is possible that the following particle will be an electron, muon, or tau neutrinos. In the mass eigenstate, the percentage of flavor mixing is constant. And this ratio can be expressed as a set of fixed parameters. These parameters denotes the neutrino oscillation and can be used to determine the likelihood of neutrino

3

oscillation. The neutrino mixing can be expressed by the following equation

$$\nu_\alpha = \sum_{i=1}^{3} U_{\alpha i} \nu_i (\alpha = e, \mu, \tau) \tag{1.1}$$

Here, ν_α denotes the type of neutrino, e denotes an electron, μ denotes a muon, and τ denotes a tau. ν_i means the mass of the neutrino, and U is the lepton mixing matrix called PMNS matrix[9].

$$U = \begin{pmatrix} 1 & 0 & 0 \\ 0 & C_{23} & S_{23} \\ 0 & -S_{23} & C_{23} \end{pmatrix} \begin{pmatrix} C_{13} & 0 & S_{13}e^{-i\delta_{CP}} \\ 0 & 1 & 0 \\ -S_{13}e^{i\delta_{CP}} & 0 & C_{13} \end{pmatrix} \begin{pmatrix} C_{12} & S_{12} & 0 \\ -S_{12} & C_{12} & 0 \\ 0 & 0 & 1 \end{pmatrix} \begin{pmatrix} 1 & 0 & 0 \\ 0 & e^{i\frac{\alpha_{21}}{2}} & 0 \\ 0 & 0 & e^{i\frac{\alpha_{31}}{2}} \end{pmatrix}$$
$$\tag{1.2}$$

where C_{ij} is $\cos\theta_{ij}$, S_{ij} is $\sin\theta_{ij}$, δ_{CP} is Dirac CP phase, α_{21} and α_{31} mean majornara CP phase. Three mixing angles, CP phase, and two mass squared differences are used to parameterize the neutrino oscillation. Only the hierarchy of mass and the CP phase have not been clearly determined as far[7].

1.3.1 Leptonic CP violation

The CP transformation means that parity transformation and charge conjugation occur simultaneously. Parity transformation refers to the process of converting a right(left)-handed coordinate system to a left(right)-handed one. Charge conjugate transformation means turning matter (antimatter) into antimatter (matter). CP symmetry means that the laws of physics do not change even when CP transformation occurs. The CP violation means this symmetry is broken. A left-handed neutrino has the same CP symmetry as a right-handed anti-neutrino. There have been no discoveries of right-handed neutrinos or left-handed anti-neutrinos in the cosmos to yet. This means that the CP symmetry is still preserved. The degree of CP violation in neutrino oscillations can be characterized by the difference in the oscillation probabilities of neutrinos and anti-neutrinos.

$$P(\nu_\mu \to \nu_e) - P(\overline{\nu_\mu} \to \overline{\nu_e}) \propto \sin\delta_{CP} \tag{1.3}$$

According to experimental evidence to date, $\delta_{CP} = -\frac{\pi}{2}$ (or $\delta_{CP} = \frac{3\pi}{2}$). Due to the fact that sine δ_{CP} is not 0, it appears as if CP is violated. In the Hyper Kamiokande laboratory currently under construction, it seems that this parameter can be measured more accurately using the neutrino beam generated by J-PARC[10].

1.3.2 Neutrino mass hierarchy

The mass hierarchy is the order of magnitude of the three neutrino masses. The mass hierarchy can be determined by measuring the oscillation probabilities according to how much material effects the neutrino beam passes through.

1.4 Proton decay

The standard model accidentally preserves the number of baryons, potentially breaking the stability of the proton, and this violation of the baryon number is an important clue to explaining the universe with more matter than antimatter. According to Grand Unified Theories, the decay of protons is predicted to exceed 10^{30} years. Hyper-Kamiokande and DUNE experiments[11] are known to have the potential to observe this degree of proton decay.

Chapter 2

Characteristics of Photomultiplier Tubes

Because of the low noise and high amplification levels of photosensors of the vacuum tube type, it is frequently employed in studies in astronomy, medicine, biology, chemistry, and physics. Photosensors of the vacuum tube type are experimental instruments that can detect weak light by the photoelectric effect. The photocathode, the multiplication component, and the anode are the three primary components of vacuum-tube-type photosensors. Popular vacuum-tube-type photosensors include the conventional PMT, MCP-PMT[12], and Hybrid PhotoDetector (HPD)[13].

2.1   Conventional Photomultiplier Tubes

A general PMT refers to a PMT of a multi-dynode structure in which the inside is vacuumed. This PMT has several dynodes, and one of its characteristics is that electrons are amplified as they pass through the dynodes in a sequential manner. External light excites electrons in the photocathode, and electrons are emitted from the photocathode into the PMT's interior. Due to the presence of an internal voltage, these photoelectrons are guided toward the first dynode, where they are converted into secondary electrons. And the secondary emitted electrons go to the next dynode, where they do the same secondary emission. Eventually, these electrons go to the anode, and the electrons become a signal which could be magnified and evaluated. The conventional PMT structure is illustrated in Fig. 2.1. The advantages of PMTs are as follows.

- Since the price per unit area is low, it is possible to configure a large area
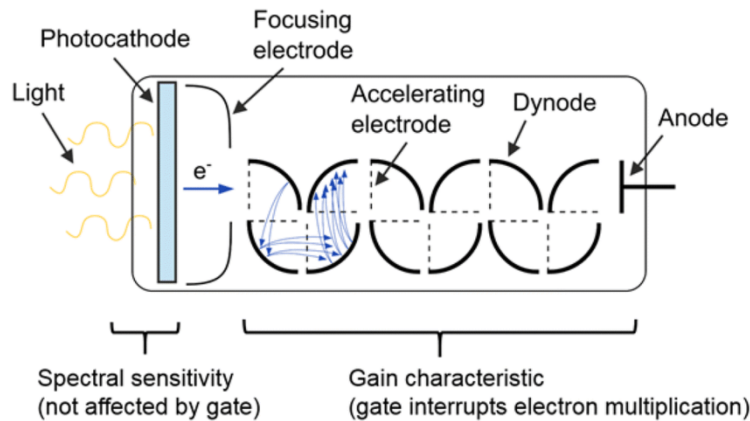
Figure 2.1: Schematic structure of the Conventional PMT[14].

PMT.

- It has a relatively high gain.

- It is very sensitive to ultraviolet and visible light.

- At low temperatures, the noise level is quite low.

- It has a high degree of linearity.

- It has a fast timing, particularly in terms of rising time.

- It has sensitivity to detect single photoelectrons.

The disadvantages of PMTs are as follows.

- It may be damaged if exposed to strong light.

- It is very sensitive to magnetic fields.

- In the infrared region, the efficiency is diminished.

- The voltage of operation is high.

2.2   Hybrid Photo-Detector(HPD)

A hybrid photodetector is a detector that amplifies photoelectrons by using a diode or a avalanche diode as part of the device. After photoelectrons are emitted

from the photocathode to the inside by external light, the emitted photoelectrons are directed to the diode by the internal voltage. Photoelectrons hitting the diode surface cause electron bombardment, which is the principle of amplification. In the case of an avalanche diode, it is further amplified with an avalanche. The structure of a HPD is shown in Figure 2.2. The benefits of HPDs over traditional PMTs are
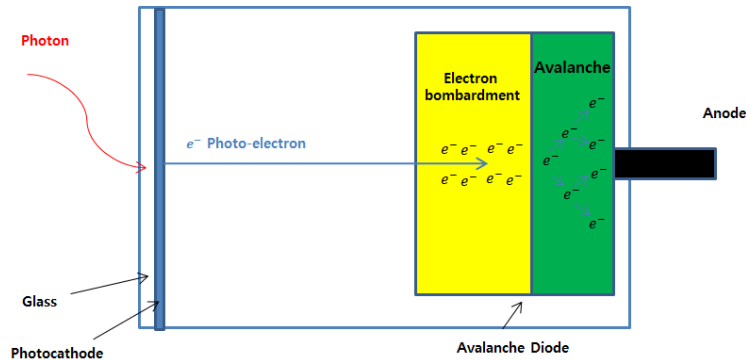
Figure 2.2: Schematic structure of the Hybrid PMT.

as follows.

- It has a high pulse height resolution and a moderate variation of amplification due to the high bombardment gain.

- Owing to the structure's simplicity, the after-pulse ratio is low.

- It has shorter transit time, transit time spread and timing resolution for the HPD are in the picosecond range.

- It is not sensitive to magnetic fields.

The disadvantages of HPDs are as follows.

- The gain is smaller than that of a standard PMT.

- The gain is significantly affected by temperature changes.

2.3   Micro Channel Plate PMT(MCP-PMT)

A micro-channel plate PMT means the structure that amplifies electrons is micro-channel plates. A micro-channel plate is a collection of miniature parallel-to-parallel

electrical amplifiers, each of which is a dynode-walled hole. After receiving external light and generating electrons from the photocathode, these electrons are accelerated to the MCP. These electrons emit secondary electrons from the wall of the channel in the MCP, and the secondary emitted electrons are continuously multiplied as they pass through the channel. The benefits of MCP-PMTs over traditional PMTs are as follows.

- Higher gain compared to its small size of a MCP.

- Fast response speed.

- It is less affected by magnetic fields.

- Relatively low power consumption.

Figure 2.3: Schematic structure of the MCP PMT[15].

2.4 Characteristics of PMTs

2.4.1 Gain

Conventional PMT

The gain is a number indicating how many electrons are amplified when one electron is generated at the photocathode and finally goes to the anode. In the case of conventional PMT, which is a step-by-step dynode structure, the gain G is expressed as follows.
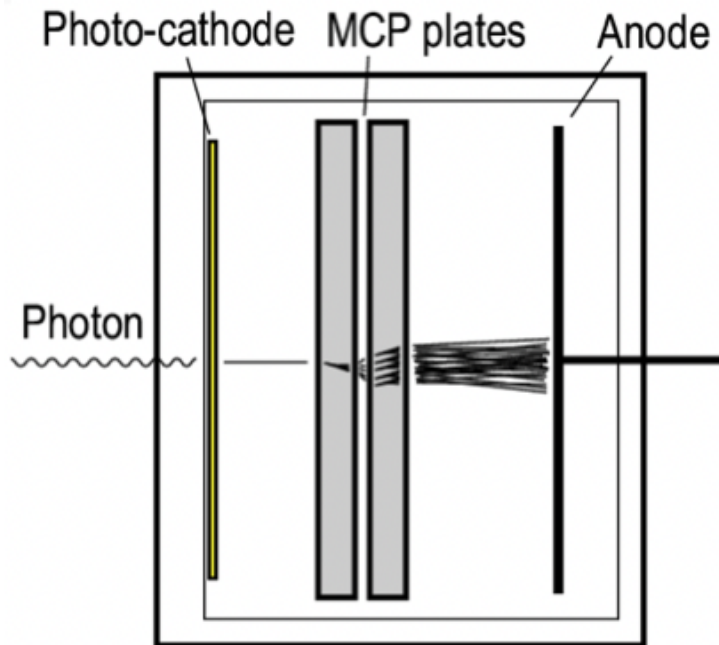
$$G = a^n (\frac{V}{n+1})^{kn} \tag{2.1}$$

Where n is the number of dynodes, a is a constant, V is applied voltage to the PMT, k is a number determined by the material and structure of the dynode. It can be seen that the gain is proportional to the power of the supply voltage.[16]

MCP-PMT

A single microchannel's current gain is expressed as follows[17].

$$G = (\frac{V}{Kn})^{mn} \tag{2.2}$$

Where n represents the number of stages along the channel, V represents the MCP-PMT's voltage, and K and m are defined by the stage length and the secondary electron emission yield of the secondary emitter. The n is proportional to the channel length and inversely proportional to the stage length. It can be seen that the gain of the MCP-PMT is also the power of the applied voltage.

HPD

The overall gain in a hybrid PMT is calculated by multiplying the electron bombardment gain by the avalanche gain. The gain of electron bombardment is the value at which the energy of electrons generated by the voltage within the PMT induces bombardment in the silicon detector, and it may be stated as follows[16].

$$G_b = \frac{(V_{pc} - V_{th})}{E_{ehp}} \tag{2.3}$$

Where G_b denotes the bombardment gain, V_{pc} is electric potential difference between the photocathode and the semiconductor, V_{th} is the threshold voltage, and

E_{ehp} is the energy needed to form an electron hole pair. If the avalanche gain is G_a, the total gain is expressed as follows.

$$G = G_b \times G_a \tag{2.4}$$

2.4.2 Timing

The timing properties of the PMTs can be an important factor depending on the physical phenomenon to be measured, for example, the decay timing of the scintillator and the timing resolution required for event reconstruction when using multiple PMTs.

Transit Time

The transit time is the time interval between when electrons are created at the photocathode and when they reach the anode. The emission time of photoelectrons from photocathode and the secondary emission of electrons from the dynode are very short, so the time characteristics of the PMT depend on the trajectory of the electrons moving inside the PMT. If the size of PMT is large, the trajectory of electrons becomes longer, so the transit time increases. When the applied voltage is increased, the electrons travel faster and the time interval between them is shortened. If the transit time is constant, it can be applied by entering the transit time as a constant, but if there is a deviation in the transit time, it is important to consider the deviation in the application of PMT. The transit time spread reveals how much variation there is in transit time. The exterior structure of the PMT is dominant since the locations of electrons created at the photocathode change based on the structure of the PMT. The photocathode of a PMT should be curved in order to decrease the transit time spread. Nonetheless, it is preferable to have a flat form in order to mount scintillators on the PMT glass component. This is supplemented by the fact that the photocathode of PMTs is generally in the form of a piano-concave with a concave interior surface.

Rising Time and Falling Time

The time interval between 10% and 90% of the peak of a single photo electron signal is called the rising time. This is the interval indicating a certain range in the time period from the time amplified electrons start entering the anode to the maximum. The falling time is defined as the time interval between 90% and 10% of the peak of a single photo electron signal. This is the interval indicating a certain range in the time period from the time majority of amplified electrons arrive at the

anode to the terminal amplified electrons arrive. In the case of conventional PMT, it is known that the falling time is 2~3 times longer than the rising time.

2.4.3   Dark Count Rate

The dark count rate is the frequency of signals equivalent to photo-electrons released from a photomultiplier tube in the absence of incoming light. Thermionic emission from the photocathode and electrode is the primary source of the dark count rate, while other minor causes include current leakage from the PMT electrode or flash emission from cosmic rays. Even at room temperature, thermo-electrons are emitted due to the low work function of the photocathode and dynode surfaces. Richardson's thermoelectric emission law can be expressed as follows.

$$I = AT^2 \times e^{\frac{-ew}{kT}} \tag{2.5}$$

Where T, I, w, e, k and A are absolute temperature, current, work function, electron charge, Boltzmann constant and a constant, respectively[16]. According to this calculation, the lower the temperature, the lower the rate of dark counts will be seen. Because the frequency of these thermionic electrons' pulses varies depending on the kind of photocathode material and is related to the photocathode's area, it may be preferable to employ a small area of the PMT at a low temperature in applications that detect extremely weak and rare light.

2.4.4   After Pulse

The photoelectric effects of the photocathode or the photocathode's thermoelectric emission should ideally induce signals from a PMT. However, during the processes of amplification, after being generated a photo-electron at the photocathode and becoming a signal at the anode, unexpected processes may occur. This process make spurious signal pulse may be noticed before and after the principal pulse. Among these often unknown pulses, some pulses that follow a set time interval are referred to as after-pulses. After-pulses may be classified into two groups. The pulses produced by the amplification structure inside the PMT in a short period of tens to hundreds nanoseconds following the primary pulse are one example. The residual quantity of gases within causes the other kind of after-pulses (not fully vacuum). When electrons are propelled toward amplifying components from the photocathode, they collide with pre-existing gases in the PMT, resulting in the formation of positive ions. These positive ions return to the photocathode and create further photoelectrons as a result of the internal voltage, and the pulses induced by

these photoelectrons constitute the second kind of after-pulses. Because the mass and charge of an ion are specified by its elements, the ion's energy and velocity are determined as well. As a result, it can be seen that the second kind of after-pulses have specific travel times. These second after pulses have a range of several hundred nanoseconds to tens of microseconds, depending on the kind of existing gases, the produced location, and the applied voltage. There are two types of after-pulse ratios. The ratio obtained by dividing the sum of charges on the after-pulses by the charge on the primary pulse is one. The number of after-pulses divided by the number of main pulses and photo-electron charges linked with the main pulse is the other[18].

2.4.5 Charge Resolution, Signal to Noise Ratio, Peak to Valley Ratio

There are two types of PMT noise, one mainly caused by thermoelectron emission generated from photocathodes and the other one by statistical fluctuations in current.

Charge Resolution

The number of electrons of a single photo-electron signal is derived as a statistical value, and the statistical distribution of the number of electrons reflects the charge resolution of the single photo-electron signal.

Signal to Noise Ratio

The signal-to-noise ratio is a number indicating the degree of noise. This parameter's definition varies by application and field. This study defines the signal-to-noise ratio as the ratio of the signal-to-noise charge ratio.

Peak to Valley Ratio

A peak to valley ratio is an indicator of how well photo-electronic noise is separated from current noise (pedestal). In a charge histogram of single photo-electrons, it refers to a value obtained by dividing the peak value of the single photo-electron by the value of the valley between the single photo-electron area and the pedestal area.

Experimental Section

Fig. 3.1 shows the schema of the PMT test setup. The PMT was shielded to prevent light leakage in a constant humidity and temperature chamber, and a function generator, a voltage supply, a pre-amplifier, a digital oscilloscope, a data acquisition (DAQ) system, two different types of analog-to-digital converters, which are FADC400 (400 MHz sampling rate Flash Analogue to Digital Converter[19]) and NGT400[20], were placed adjacent to the chamber. Two identical forms of MCP-PMTs were studied. All measurements were performed around 30 minutes after applying voltage to the PMT in order to stabilize the PMT. The FADC400 digitizes and stores all information at regular time intervals for the raw signal at each window, like an oscilloscope. Due to its properties, it was utilized when factors required precise charges or needed whole window information. The NGT400 stores the pulse information in a set gate and additionally calculates the number of pulses, total measurement time, etc. But it can not reconstruct the event. For this reason, NGT400 was only used to find specific information or to measure the dark count rate. The PMT is seen in Fig. 3.2.

3.1   Rising and Falling time

The rising and falling times of the single photon electron(SPE) waveforms were determined using a digital oscilloscope (Waverunner 610zi LeCroy[21]) without amplification at room temperature. A threshold of 3 mV was applied, which approximately match to an estimated 0.25 single photo-electron (SPE) amplitude. And during the analysis, if there were amplitude of signals of 30 mV or heigher in the window, the window was rejected and rest windows were averaged to calculate the rising and falling times.

3.2   Gain

The gain measurement was determined using a dim Light Emitting Diode (LED) (light with a wavelength of 505 nm) and the FADC400. The LED was linked to the function generator, and the light from the LED is delivered to the PMT via an optical fiber. An oscilloscope was used to verify that the intensity and frequency of the LED were tuned to the number of signals corresponding to single photo-electrons of the PMT output.

3.3   Dark Count Rate

No light source is used to measure the dark count rate and its temperature dependancy. Instead, a 10-fold amplification pre-amplifier is used, and a thermocouple is attached to monitor the temperature while receiving data from the NGT400. The dark count rate measures the noise ratio in the absence of any light, so the external light must be completely blocked. In order to check whether external light is completely blocked, it was confirmed that there is no difference in the dark count rate by comparing the state in which there is light outside the chamber and the state in which there is no light. Also, to check whether the experiment structures attached or installed on the PMT have an effect, the dark count rate with and without the structures was checked.

3.4   Charge Resolution, Peak to Valley Ratio, Signal to Noise Ratio

The charge resolution, peak to valley ratio and signal to noise ratio measurement were determined using a dim LED light, the NGT400, and amplification by ten times with a pre-amplifier.

3.5   After Pulse

A bright LED light (372 nm wavelength and intensity that can produce charge of hundreds of photo-electrons signals), the FADC400, and a digital oscilloscope were used to measure after-pulses. Electronics and a data acquisition system that can store information such as charge and the timing of pulses are necessary in order to count the after-pulses. Since the after-pulse is dispersed between tens of nanoseconds and tens of microseconds, the sampling rate must be a few nanoseconds or

less, and electronics must be able to store events with an event window of tens of microseconds. The LED source must also be adjusted to a suitable period by setting the frequency such that one main pulse of PMT's output signal occurs in tens of microseconds in line and another LED sequence does not arrive prior to the after pulses. In addition, as there may be a fast after pulse in tens to hundreds of nanoseconds after the main pulse of the PMT output, a waveform that only persists for a brief period must be chosen in the function generator's option for the LED source. The pulse width of the pulsed wave should be adjusted to its smallest achievable value. In this manner, the main pulse and the fast after-pulse are separated in the PMT output signals. And also, the intensity of the LED was adjusted to provide the PMT's output signal of several hundred photoelectrons.
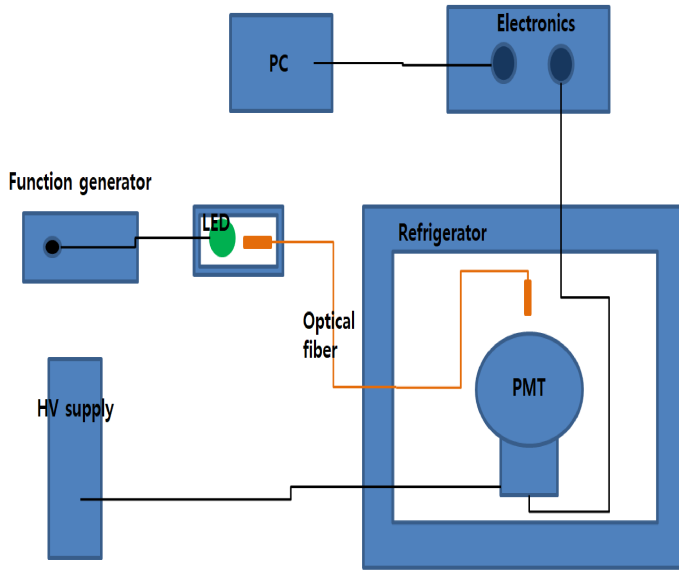
Figure 3.1: Schematic diagram of the PMT test Setup.

Figure 3.2: The 20 inch MCP PMT.

Chapter 4

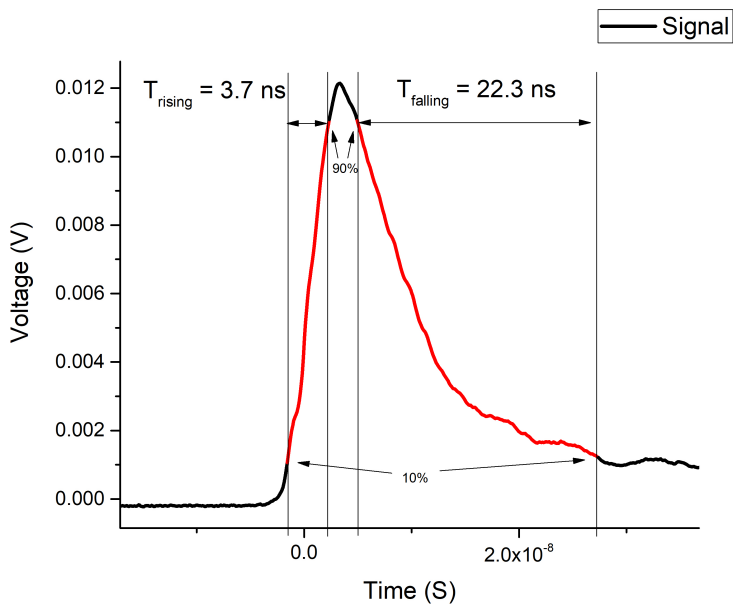# Result and Discussion

4.1 Rising and Falling time

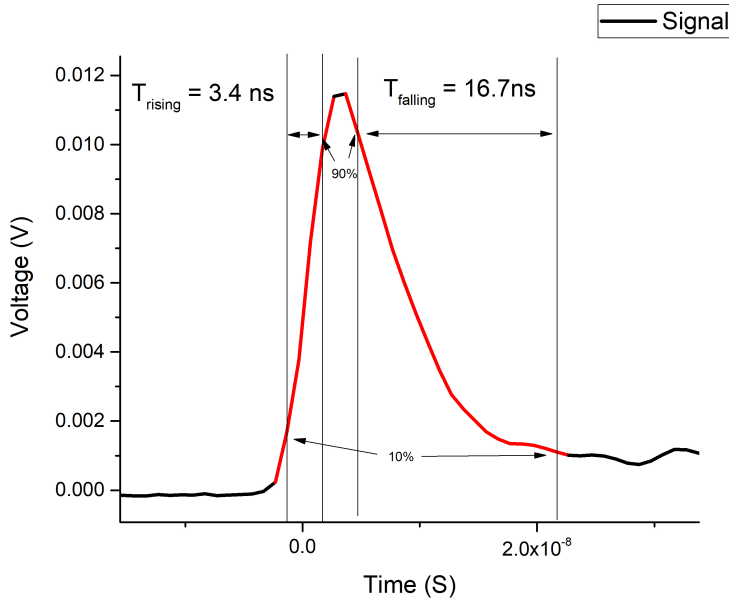Figure 4.1: 1st PMT's Rising and Falling Time

Figure 4.2: 2nd PMT's Rising and Falling Time

The rising and falling times of the first PMT are 3.7 ns and 22.3 ns, respectively, and the rising and falling times of the second PMT are 3.4 ns and 16.7 ns, respectively as shown in Fig. 4.1 and Fig. 4.2.

4.2 Gain

4.2.1 Gain

The measured charge distributions of the single photo-electrons are illustrated in Fig. 4.3. In Fig. 4.3, the peak of the SPE at the point where the average values become 42.85 ADC to the 1st PMT and 36.37 ADC to the 2nd PMT. The ADC means digital value of corresponding analogue input without dimensions, and the front of it is a pedestal area acquired by the intrinsic noises of PMT and electronics. The pedestal region is fitted with an exponential function, and the SPE region is
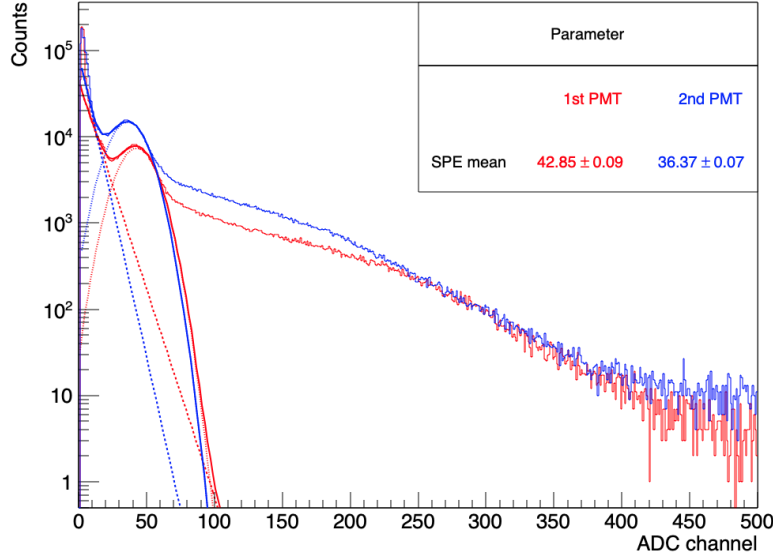
Figure 4.3: Single Photo-electron charge distributions of two PMTs

fitted with a Gaussian function. The following formula is to express the gain[22].

$$G = \frac{(<SPE> - <PED>) \times I \times T}{A_{gain} \times e} \qquad (4.1)$$

The $\langle SPE \rangle$ is the ADC value of the peak obtained by Gaussian fitting of the SPE ("SPE mean" in the Fig. 4.3), and the $\langle PED \rangle$ is the ADC value at the peak of the PED (pedestal) which is zero in Fig. 4.3. ($\langle SPE \rangle$ - $\langle PED \rangle$) are set to 42.85, 36.37. I is the value of volts for one ADC channel ($\frac{1}{1024}$ volts) divided by 50 Ω of ADC resistance. T represents the sampling time of the ADC channel and is 2.5 ns. A_{gain} is a value related to how much amplification is applied and here is 1.2. e is the electric charge 1.6×10^{-19} C. The fist and second PMT's gains in Fig. 4.3 are 1.09×10^7 (at 1800V), 9.25×10^6 (at 1900V).

4.2.2 Gain Parameter

As demonstrated in Equation 2.2, gain is proportional to the multiplier of the applied voltage. To verify this multiplier parameter, the gain was determined in relation to the applied voltage and fitted as a function of the multiplier of the applied voltage, as shown in Figure 4.4. For the two PMTs, the gain was found to be pro-

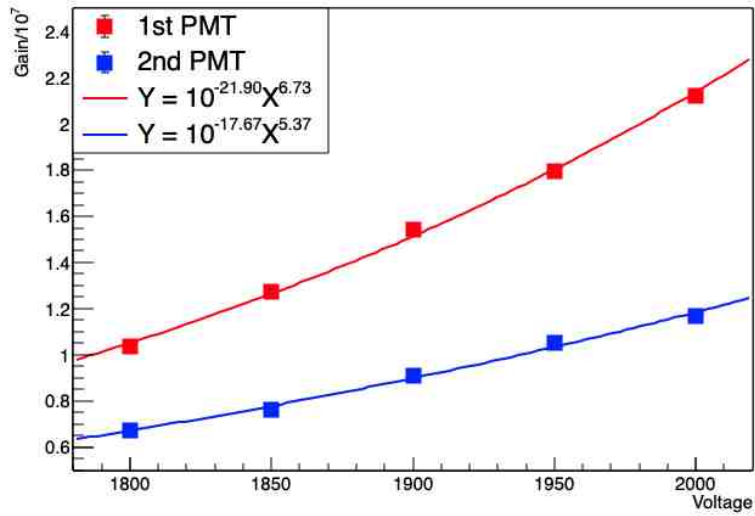portional to the 6.73 and 5.37 powers of the voltage, respectively.

Figure 4.4: The gain values according to the voltage
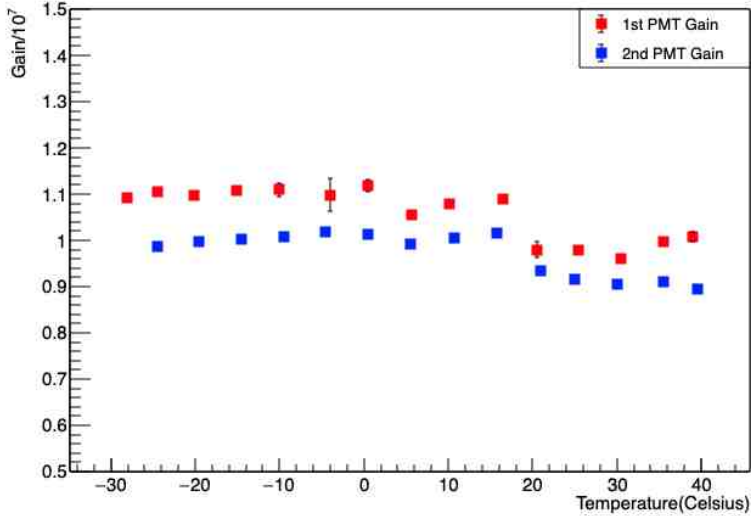
4.2.3 Gain as a function of temperature

Figure 4.5: The gain values according to the temperature of two PMTs

To determine how much the gain changes with temperature, the gain was measured at various temperatures, the results of which are given in Fig. 4.5. It is known that the gain decreases as the temperature increases, but there was no substantial difference in the temperature range between $-30°C$ and $40°C$.

4.3 Dark Count Rate

Dark Count Rate

To measure the dark count rate, the threshold was lowered as much as possible in the absence of any light, and noise was measured. From the histogram in Fig. 4.6, the entry of the pedestal was subtracted from the valley where the single photoelectron area and the pedestal area met, and the total entry to the entry of photoelectrons was obtained, then the number of pulses was multiplied and the calculated time was divided.

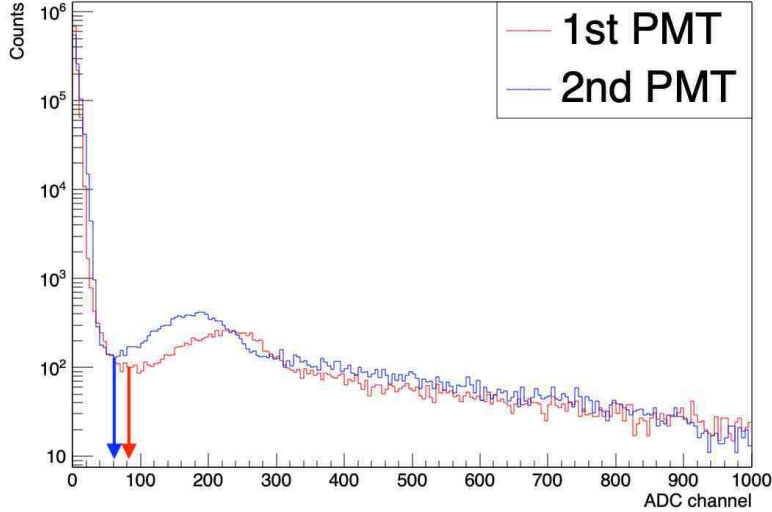$$R_{DC} = \frac{E_{PE}}{E_{Total}} \times N_{Signal}/T \tag{4.2}$$

Figure 4.6: Single Photo-electron Charge distributions of two PMTs with NGT400

Table 4.1: Dark count ratio

	Number of pulses	Total time	PE ratio
1st PMT	5.42×10^7	$71s$	0.016
2nd PMT	7.20×10^7	$71s$	0.021

In Equation 4.3, R_{DC} denotes the dark rate and $\frac{E_{PE}}{E_{Total}}$ denotes the photoelectrons entry ratio. N_{signal} denotes the total number of pulses, while T is the total time. The dark rate obtained in this method, the first PMT's dark count rate is 12.4 kHz and the second PMT's dark count rate is 21.3 kHz.

4.3.1 Dark count rate as a function of temperature

Temperature can have a substantial influence on the dark count rate since photo-electron noise in the absence of light is mostly due to thermionic emission from the photocathode. As can be see in Fig. 4.7, the dark count rate rapidly increases when the temperature exceeds 30 degrees. There is little variation below that temperature.
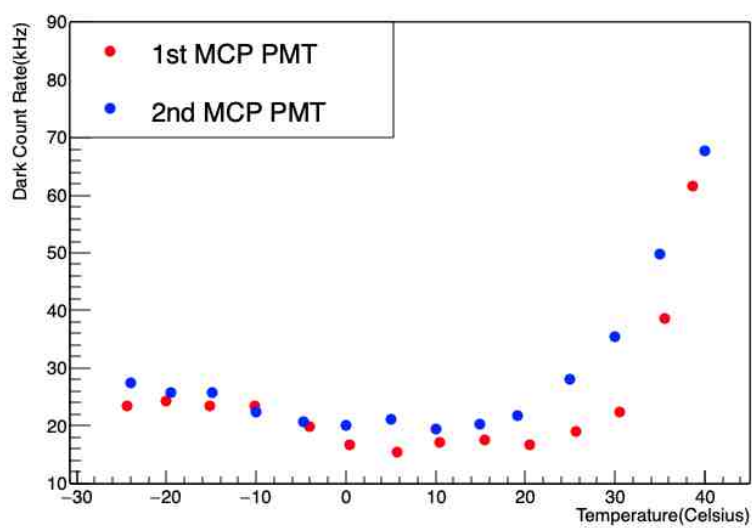
Figure 4.7: Two PMTs's Dark count rate as a function of temperature

4.4 After pulse

4.4.1 After pulse timing

Table 4.2: After pulse timings.

After pulse	Reference	1st PMT	2nd PMT
1st After pulse	215 ns	123 ns	123 ns
2nd After pulse	841 ns	920 ns	881 ns
3rd After pulse	3069 ns	3541 ns	3326 ns
4th After pulse	4431 ns	5081 ns	5012 ns

As shown in Figure 4.8 and 4.9, the after-pulse timings of the first PMT were 123 ns, 920 ns, 3541 ns, and 5081 ns, respectively, and the after-pulse timings of the second PMT were 123 ns, 881 ns, 3326 ns, and 5012 ns, respectively. These values are shown in Table 4.1 compared to the after-pulse timing of the Fig. 4.10.

4.4.2 After pulse count ratio

The after-pulse count ratio can be expressed as follows

Table 4.3: After pulse counts.

Counts	1st PMT	2nd PMT
Main pulse	220000	230000
1st After pulse	1000000	900000
2nd After pulse	390000	410000
3rd After pulse	200000	250000
4th After pulse	100000	120000

$$APR_N = \frac{N_{AP}}{N_{MP} \times Q_{MP}} \times 100 \tag{4.3}$$

Where APR_N is after-pulse count ratio, N_{AP} is the number of after-pulses, N_{MP} is the number of main pulses, Q_{MP} is the number of photoelectrons in the main pulse.
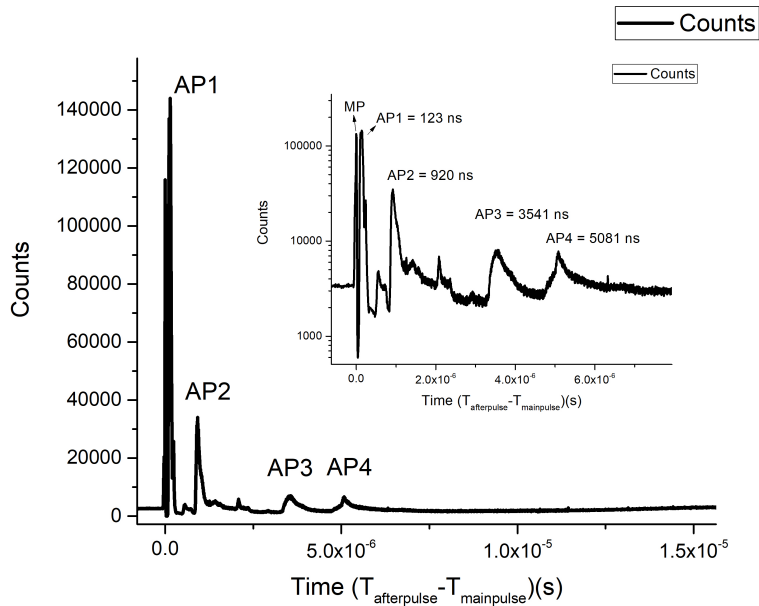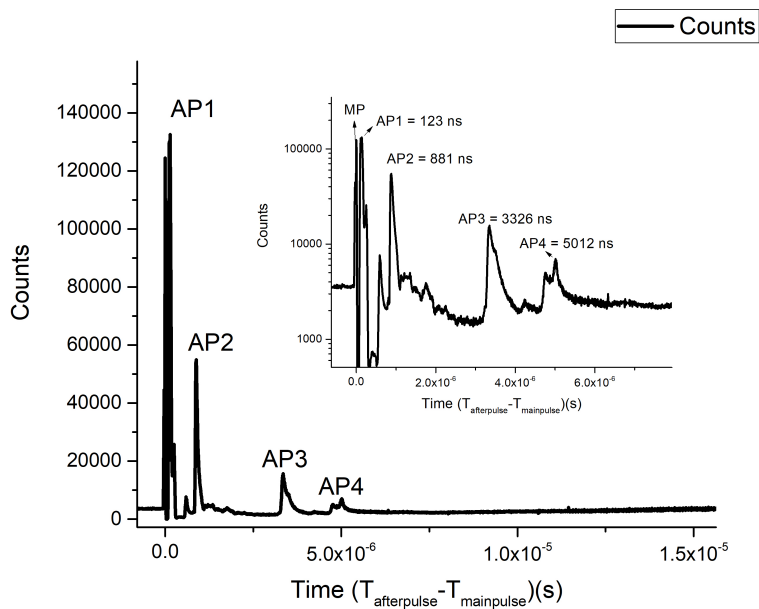
Figure 4.8: The pulse timings of the 1st PMT.

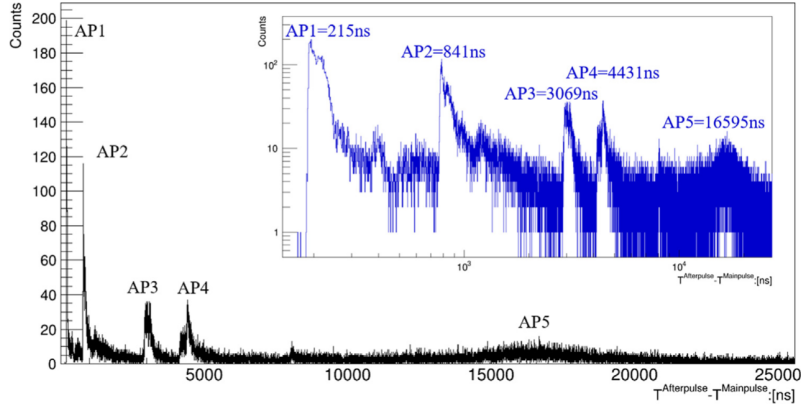Figure 4.9: The pulse timings of the 2nd PMT.

Figure 4.10: After pulse timings from other research[18].

Q_{MP} was obtained by dividing the mean ADC of the PMT output signal by a single photoelectron mean ADC. Q_{MP} of the first PMT corresponds to 229 and Q_{MP} of the second PMT corresponds to 214. Using equation 4.3 and the values in Table 4.3, the after-pulse count ratio of the first PMT was $(3.35 \pm 1.17)\%$, and the after-pulse count ratio of the second PMT was $(3.41 \pm 1.33)\%$. The errors of after-pulse count ratios were calculated conservatively, and most of the source of the errors came from the standard deviation of the charge of the single photoelectron. The charge distributions of the after-pulses are shown in Appendix A.

4.4.3 After pulse charge ratio

Fig. 4.11 and 4.12 were obtained by averaging event windows. The data was obtained by giving an LED source with PMT response of hundreds of photoelectrons. After taking data with a digital oscilloscope, additionally 3 mV threshold was applied to the area where the after-pulse was visible to reduce noise effect. The after-pulse charge ratio is obtained as follows.

$$APR_Q = \frac{Q_{AP}}{Q_{MP}} \times 100 \tag{4.4}$$

Where APR_Q is after-pulse charge ratio, Q_{AP} is after-pulses's total charge, Q_{MP} is

Table 4.4: After pulse charge distribution

Area(v·s)	1st PMT(v·s)	2nd PMT(v·s)
Main pulse	3.1×10^{-8}	4.1×10^{-8}
1st After pulse	2.4×10^{-9}	1.8×10^{-9}
2nd After pulse	8.9×10^{-10}	1.1×10^{-9}
3rd After pulse	1.8×10^{-10}	3.4×10^{-10}
4th After pulse	1.5×10^{-10}	1.1×10^{-10}

main pulse's charge. Table 4.4 shows the area of the pulses in Fig. 4.12 and 4.13, and the after-pulse charge ratio was obtained using Equation 4.4. The after-pulse charge ratio of the first PMT was 11.7 %, and the after-pulse charge ratio of the second PMT was 8.2 %.
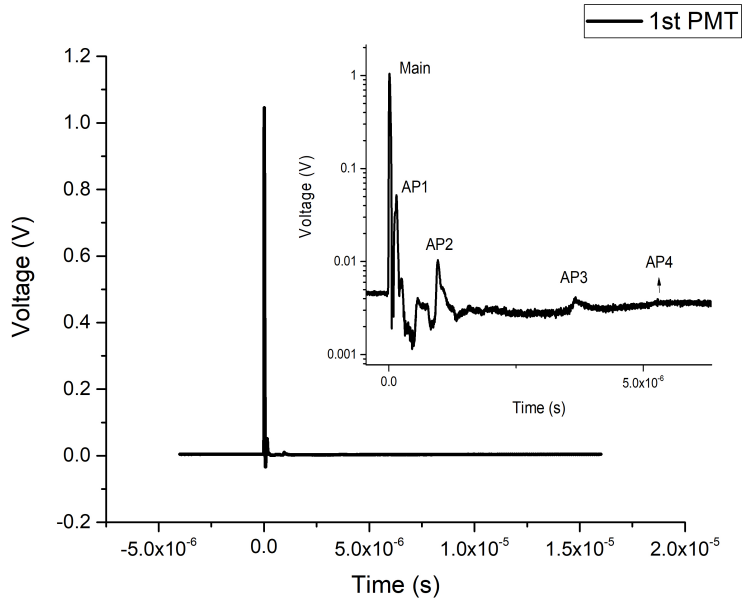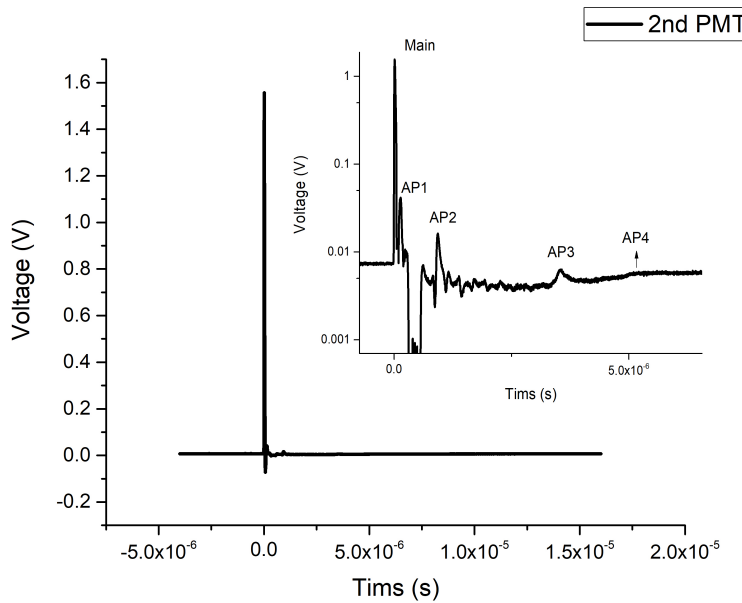
Figure 4.11: The LED response of the1st PMT.

Figure 4.12: The LED response of the 2nd PMT.

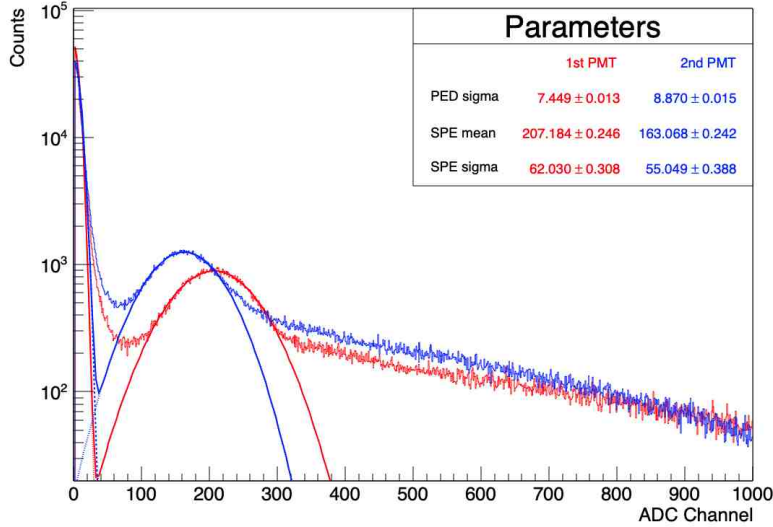## 4.5 Charge Resolution, Peak to Valley Ratio, Signal to Noise Ratio

Figure 4.13: Single Photo-electron Charge distributions of two PMTs with a LED source and NGT400.

$$ER = \frac{SPE_{mean}}{SPE_{sigma}} \times 100 \tag{4.5}$$

$$P/V = \frac{SPE_{peak}}{SPE_{valley}} \tag{4.6}$$

$$S/N = \frac{SPE_{mean}}{PED_{sigma}} \tag{4.7}$$

The Fig. 4.13 is a graph of charge distribution of a single photoelectron obtained using a LED source, a preamplifier, and the NGT400. In equation 4.5, SPE_{mean}, SPE_{sigma} are SPE mean and SPE sigma in Fig. 4.13 respectively. In equation 4.6, SPE_{peak} and SPE_{valley} are peak's height and the valley height of between pedestal and signal region in Fig. 4.13 respectively. In equation 4.7, SPE_{mean} and PED_{sigma} are SPE mean and PED sigma in Fig. 4.13 respectively. The energy resolutions of the first and second PMTs are 29.94% and 33.75% respectively. The P/V of two PMTs are 5.0 and 2.74, respectively. The signal to noise ratios of two PMTs are

30

27.81 and 18.38 respectively.

4.6   Summery

Table 4.5 compares the data provided by NNVT, the organization that developed and tested this PMT. When the test results are compared to the reference values in the two PMTs, the charge resolution and rising time are comparable. The gain in the first PMT was significantly greater than predicted, whereas the gain in the second PMT was little less than expected. In general, the gain has a wide range of error, and these number can be considered to be within the error range. Regarding the dark rate, the first PMT was roughly identical to the predicted value, while the second PMT was higher than expected. Both the after-pulse ratio and falling time were much greater than predicted for two PMTs. The ratio of peak to valley was lower than expected. In Hyper Kamiokande, the dark count rate of HQE B&L PMT, a candidate for Hyper Kamiokande internal detector, was 8.3 kHz (10^7 gain, at 13° C)[7]. Therefore the dark count rate was slightly higher than that. Table 4.6 compares the requirements of the Hyper Kamiokande's internal detector with the experimental results of these PMTs because KNO has a water tank of the same size as the Hyper Kamiokande and has many similarities. Because gain may be raised by increasing the voltage, the charge resolution, gain, and after-pulse ratio appear to meet the requirements.

	1st PMT reference	1st PMT result	2nd PMT reference	2nd PMT result
Voltage	1802 V	1800 V	1875 V	1900 V
Charge resolution	28.77%	29.94%	28.45%	33.75%
Gain	9.92×10^6	1.09×10^7	9.94×10^6	9.25×10^6
After-pulse rate	0.36%(count)	(3.35 ± 1.17)%(count), 11.7%(charge)	0.58%(count)	(3.41 ± 1.33)%(count), 8.2%(charge)
Dark count rate	12.15 kHz	12.31 kHz	12.91 kHz	21.30 kHz
Rising time	3.65 ns	3.7 ns	3.56 ns	3.4 ns
Falling time	11.89 ns	22.3 ns	10.32 ns	16.7 ns
Peak to valley ratio	9.3	5.0	10.9	2.7

Table 4.5: Comparison of the result with the NNVT's report

Requirements	Value	1st PMT	2nd PMT
Charge resolution	50% (Typ.)	29.94%	33.75%
Gain	$10^7 \sim 10^8 (Typ.)$	$1.09 \times 10^7 (at\,1800V)$	$9.25 \times 10^6 (at\,1900V)$
Afterpulse rate	5%(Max.)	(3.35 ± 1.17)%(counts)	(3.41 ± 1.33)%(counts)

Table 4.6: Comparison of the result with the requirements of the Hyper Kamiokande inner photosensor

Chapter 5

Conclusion

To detect water Cherenkov radiation generated by neutrino interactions or proton decays, a large water tank and a large number of large-diameter PMTs deep underground are required. Future large-scale neutrino studies will rely heavily on understanding the features of large-size photosensors such as 20-inch MCP-PMTs, as well as developing accurate characterization techniques. With our study, we were able to acquire findings that were comparable to those obtained by other researchers. The gain, charge resolution, rising time, dark rate, and signal-to-noise ratio of the two PMTs were comparable to those obtained in the previous work, but the falling time and after-pulse ratio were somewhat bigger. The dark count rate according to temperature was relatively stable when the temperature was low, but increased exponentially when the temperature was increased by more than 30 degrees. The change in gain according to temperature was relatively small. After pulse charge and count ratio were found to be larger than in other study. Given that it is planned to be employed in the KNO, which is proposed to be created in a similar form to Hyper Kamiokande, the charge resolution, gain, and after pulse count ratio may be deemed to match the criteria for an inner detector in Hyper Kamiokande. Therefore, it can be considered suitable for the KNO. These PMTs will be investigated further in the near future for further features. Finally, the method developed in this study will serve as the basis for future research.

Appendix A

After-pulse charge distribution

This appendix shows the charge distribution of the after-pulses. The time region corresponding to each after-pulse was roughly determined, and the charge distribution was shown for each of the four after-pulses. A charge distribution was obtained in the same time range as an after-pulse time range in a part close to the after-pulse time domain, and this was used as a background charge distribution. The background charge distribution was subtracted from the charge distribution of the after-pulse region. The background distribution was scaled appropriately so that over-subtraction does not occur.

It can be seen that the first after-pulse of the first PMT and the second after-pulse of the second PMT have a relatively wide distribution. It is difficult to draw conclusions about the after-pulse charge distribution, so further detailed studies may be needed.
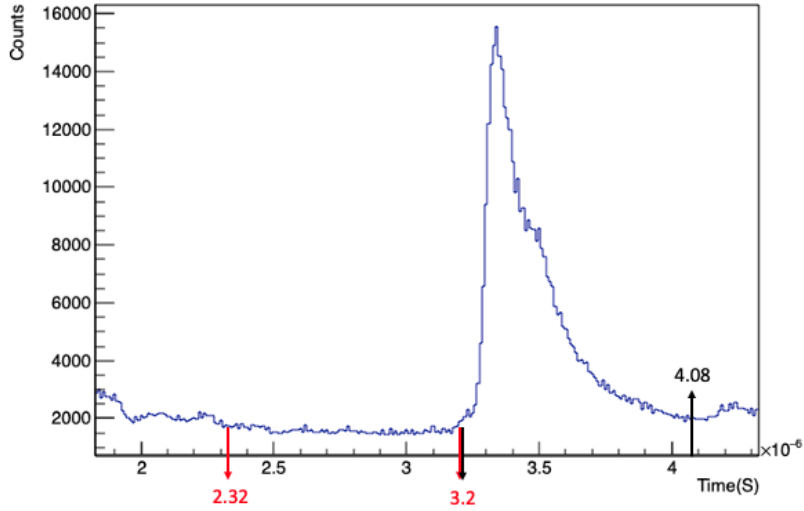
Figure A.1: An example of setting background. The background charge distribution from 2.32 to 3.2 microseconds was subtracted from the afterpulse charge distribution from 3.2 to 4.08 microseconds in this case.
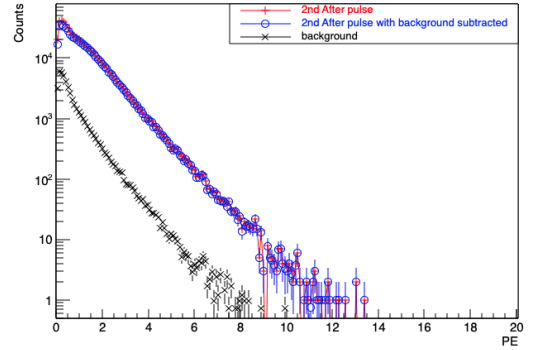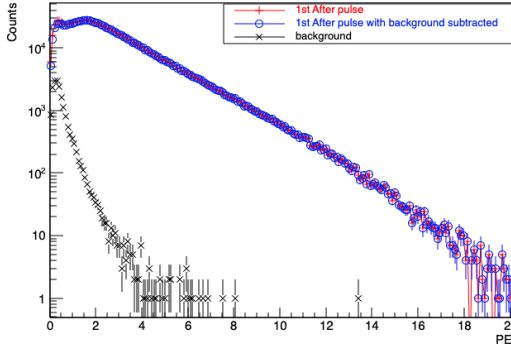
A.1 1st PMT's after-pulse charge distribution

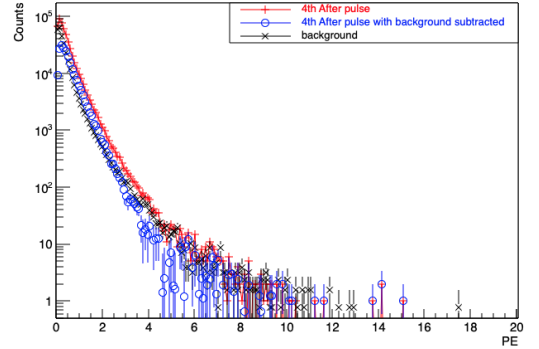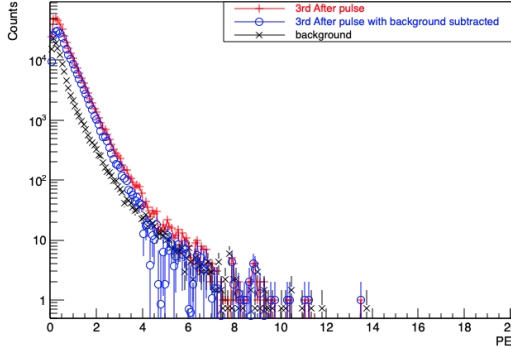| Time region	After pulse	Background
1st After pulse	40 ~ 200 *ns*	315 ~ 478 *ns*
2nd After pulse	815 ~ 1190 *ns*	1190 ~ 1565 *ns*
3rd After pulse	3315 ~ 4065 *ns*	3065 ~ 3315 *ns*, 4065 ~ 4565 *ns*
4th After pulse	4690 ~ 5815 *ns*	5815 ~ 6940 *ns*

Table A.1: The timing areas of the after-pulses and the background areas of the 1st PMT.

A.2 2nd PMT's after-pulse charge distribution

(a) 1st PMT's 1st after pulse charge distribution

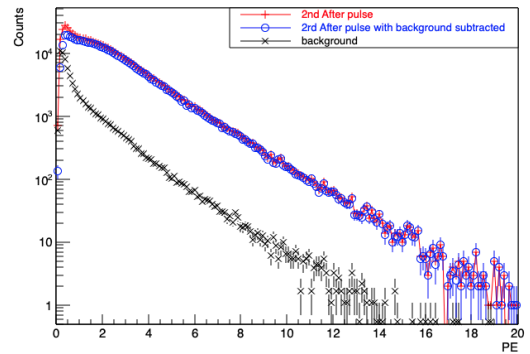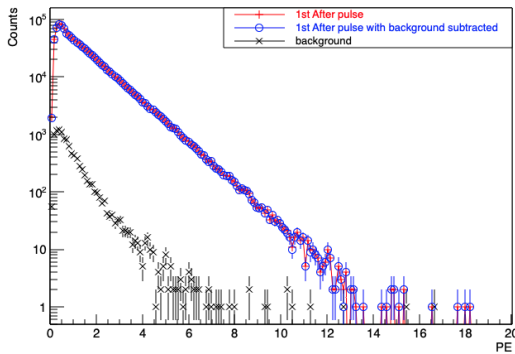

(b) 1st PMT's 2nd after pulse charge distribution

(c) 1st PMT's 3rd after pulse charge distribution

(d) 1st PMT's 4th after pulse charge distribution

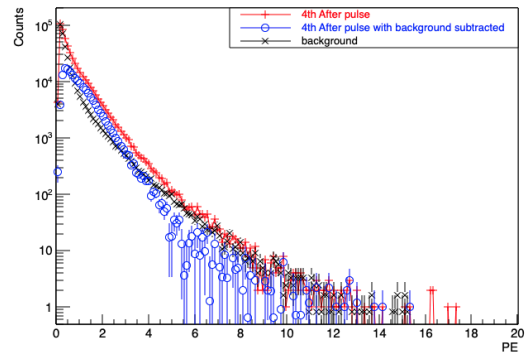Figure A.2: Charge distributions of the after-pulses of the 1st PMT.

Time region	After pulse	Background
1st After pulse	63 ~ 200 *ns*	325 ~ 463 *ns*
2nd After pulse	825 ~ 1075 *ns*	1075 ~ 1325 *ns*
3rd After pulse	3200 ~ 4075 *ns*	2325 ~ 3200 *ns*
4th After pulse	4575 ~ 5575 *ns*	5575 ~ 6575 *ns*

Table A.2: The timing areas of the after-pulses and the background areas of the 2nd PMT.

35

(a) 2nd PMT's 1st after pulse charge distribution (b) 2nd PMT's 2nd after pulse charge distribution

(c) 2nd PMT's 3rd after pulse charge distribution (d) 2nd PMT's 4th after pulse charge distribution

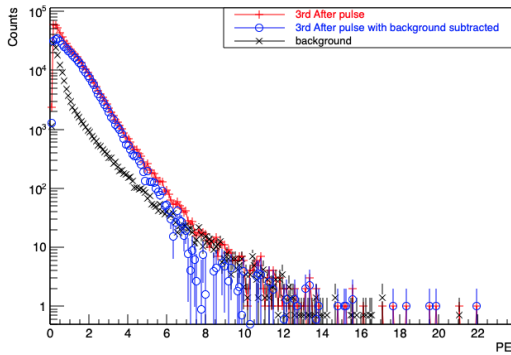Figure A.3: Charge distributions of the after-pulses of the 2nd PMT.

Bibliography

[1] Hyper-Kamiokande proto Collaboration, Ke Abe, Ke Abe, SH Ahn, H Aihara, A Aimi, R Akutsu, C Andreopoulos, I Anghel, LHV Anthony, et al. Physics potentials with the second hyper-kamiokande detector in korea. *Progress of Theoretical and Experimental Physics*, 2018(6):063C01, 2018.

[2] S. Fukuda, Y. Fukuda, T. Hayakawa, E. Ichihara, M. Ishitsuka, Y. Itow, T. Kajita, J. Kameda, K. Kaneyuki, S. Kasuga, et al. The super-kamiokande detector. *Nuclear Instruments and Methods in Physics Research Section A: Accelerators, Spectrometers, Detectors and Associated Equipment*, 501(2):418–462, 2003.

[3] A. Bellerive, J.R. Klein, A.B. McDonald, A.J. Noble, and A.W.P. Poon. The sudbury neutrino observatory. *Nuclear Physics B*, 908:30–51, 2016. Neutrino Oscillations: Celebrating the Nobel Prize in Physics 2015.

[4] J V Jelley. Cerenkov radiation and its applications. *British Journal of Applied Physics*, 6(7):227–232, jul 1955.

[5] https://physicsopenlab.org/2016/04/24/diy-cherenkov detector/

[6] MG Aartsen, M Ackermann, J Adams, Juan A Aguilar, M Ahlers, M Ahrens, D Altmann, K Andeen, T Anderson, I Ansseau, et al. Astrophysical neutrinos and cosmic rays observed by icecube. *Advances in Space Research*, 62(10):2902–2930, 2018.

[7] H Abe, Ke. Abe, Hiroaki Aihara, Akihisa Aimi, Ryosuke Akutsu, C. Andreopoulos, Im Anghel, Lauren H.V. Anthony, M. G. Antonova, et al. Hyperkamiokande design report. *arXiv: Instrumentation and Detectors*, 2018.

[8] https://indico.cern.ch/event/773605/contributions/3498145/attachments/1899 824/3135645/NUFACT2019_-_KNO_Report_20190830.pdf.

[9] Claudio Giganti, Stéphane Lavignac, and Marco Zito. Neutrino oscillations: The rise of the PMNS paradigm. *Prog. Part. Nucl. Phys.*, 98:1–54, 2018.

[10] Shoji Nagamiya. Introduction to J-PARC. *Progress of Theoretical and Experimental Physics*, 2012(1), 10 2012. 02B001.

[11] DUNE collaboration et al. Deep underground neutrino experiment (dune): Far detector technical design report. volume i. introduction to dune. *Journal of Instrumentation*, 15(8), 2020.

[12] VV Anashin, PM Beschastnov, VB Golubev, LA Mironenko, AA Salnikov, and SI Serednyakov. Photomultipliers with microchannel plates. *Nuclear Instruments and Methods in Physics Research Section A: Accelerators, Spectrometers, Detectors and Associated Equipment*, 357(1):103–109, 1995.

[13] Yasuhiro Nishimura. Hybrid photo-detectors for the hyper-kamiokande project. *International Workshop of New Photo-detectors*, 2012.

[14] Raphael Mansmann, Timothy A. Sipkens, Jan Menser, Kyle J. Daun, Thomas Dreier, and Christof Schulz. Detector calibration and measurement issues in multi-color time-resolved laser-induced incandescence. *Applied Physics B*, 125(7):126, 2019.

[15] https://indico.in2p3.fr/event/1697/contributions/21143/attachments/17274/211 86/lehmann_05may2010_PNG.pdf.

[16] Hamamatsu Photonics. *Photomultiplier tubes*. Hamamatsu, 2000.

[17] Illes P. Csorba. Current gain parameters of microchannel plates. *Appl. Opt.*, 19(22):3863–3866, Nov 1980.

[18] Qi Wu, Sen Qian, Lishuang Ma, Jingkai Xia, Bayarto K. Lubsandorzhiev, Zhigang Wang, Yao Zhu, Haitao Li, Nikita Ushakov, Andrei Sidorenkov, Qianyu Hu, Jianning Sun, and Shuguang Si. Study of after-pulses in the 20-inch hqe-mcp-pmt for the juno experiment. *Nuclear Instruments and Methods in Physics Research Section A: Accelerators, Spectrometers, Detectors and Associated Equipment*, 1003:165351, 2021.

[19] NOTICE. *FADC400*. NOTICE, http://www.noticekorea.com/?p=2418.

[20] NOTICE. *ngt400*. NOTICE, http://www.noticekorea.com/?p=2725.

[21] Teledyne lecroy. *WaveRunner® 6 Zi Oscilloscopes*. Teledyne lecroy, https://www.valuetronics.com/pub/media/vti/datasheets/LeCroy

[22] S. Aiello, S.E. Akrame, F. Ameli, E. G. Anassontzis, M. Andre, G. Androulakis, M. Anghinolfi, G. Anton, M. Ardid, J. Aublin, et al. Characterisation of the hamamatsu photomultipliers for the KM3net neutrino telescope. *Journal of Instrumentation*, 13(05):P05035–P05035, may 2018.

대구경 마이크로채널판 광전자증배관의 특성 연구

김건우

경북대학교 대학원 물리학과
(지도교수 김홍주)

(초 록)

체렌코프 방사선이란 전하가 있는 입자가 매질 안에서 진행할 때의 속도가 빛의 속도보다 빠를 때 생성되는 매질의 전자기파에 의하여 빛의 고리가 만들어지며 퍼져나가는 방사선을 말한다. 고에너지의 중성미자에 의한 체렌코프 방사선을 관측하기 위해서는 매우 많은 양의 매질과 대면적의 광센서가 필요하다. KNO는 한국에서 중성미자를 검출하기 위해 제안된 프로젝트인데 커다란 물탱크에 수만개의 광센서를 지하깊은 곳에 설치하는 검출기이다. 20인치 구경의 마이크로채널판 광전자증배관는 KNO에서 사용될 광센서 후보 중 하나인데 넓은 광면적과 높은 광수집 효율성을 특징으로 한다. 이와같은 대면적의 광전자증배관에 대한 특성을 면밀히 살펴보는 것은 KNO나 다른 체렌코프 방사선을 관측하는 실험에서 중요한 연구이다. 우리는 20인치 2개의 마이크로채널판 광전자증배관의 특성을 연구해 왔으며 단일 광전자의 전하량 레졸루션, 신호 대 잡음 비율, 암신호비율, 에프터펄스 비율 , 타이밍 특성 등을 측정하였다. 또한 이러한 측정값을 얻기 위한 방법들 또한 테스트 되었고 고안되었다. 마지막으로 우리는 이 특성들의 측정값을 이전의 연구와 비교해보았다.